Interfacial Micro-currents in Continuum-Scale Multi-Component Lattice Boltzmann Equation Hydrodynamics.

HALLIDAY, Ian <http://orcid.org/0000-0003-1840-6132>, LISHCHUK, Sergey <http://orcid.org/0000-0002-9989-765X>, SPENCER, Timothy <http://orcid.org/0000-0003-1135-4042>, BURGIN, Kallum and SCHENKEL, Torsten <http://orcid.org/0000-0001-5560-1872>

Interfacial Micro-currents in Continuum-Scale Multi-Component Lattice Boltzmann Equation Hydrodynamics.

I. Halliday, S. V. Lishchuk, T. J. Spencer, K. Burgin and T. Schenkel.

Materials & Engineering Research Institute, Sheffield Hallam University, Howard Street, S1 1WB, UK

Corresponding Author: I. Halliday
Email address: i.halliday@shu.ac.uk
Telephone: (+44) 114 225 3045
Fax: (+44)114 225 3501

Abstract

We describe, analyse and reduce micro-current effects in one class of lattice Boltzmann equation simulation method describing immiscible fluids within the continuum approximation, due to Lishchuk et al. (Phys. Rev. E 67 036701 (2003)). This model's micro-current flow field and associated density adjustment, when considered in the linear, low-Reynolds number regime, may be decomposed into independent, superposable contributions arising from various error terms in its immersed boundary force. Error force contributions which are rotational (solenoidal) are mainly responsible for the micro-current (corresponding density adjustment). Rotationally anisotropic error terms arise from numerical derivatives and from the sampling of the interface-supporting force. They may be removed, either by eliminating the causal error force or by negating it. It is found to be straightforward to design more effective stencils with significantly improved performance.

Practically, the micro-current activity arising in Lishchuk's method is reduced by approximately three quarters by using an appropriate stencil and approximately by an order of magnitude when the effects of sampling are removed.

Keywords

PACS number(s) : 47.11.-j
Keywords : lattice Boltzmann, body force

1 Introduction

Since the work of Gunstensen and Rothman [1], several multi-component lattice Boltzmann equation (MCLB) methods have been developed. Broadly, a variant may be classified by the physical content of its fluid-fluid interface algorithm. Where the kinematics of phase separation must be considered, free–energy methods [2], [3] and their thermodynamically consistent extensions, due to Wagner and co–workers [4], [5], [6], based, as they are, on the Cahn–Hilliard theory, are appropriate. For workers with a background in molecular simulation, the Shan–Chen method [7] is a natural choice. In this work we consider the MCLB interface of Lishchuk et al. [8], which is adapted to completely arrested coalescence i.e. to completely immiscible fluids, considered in the continuum approximation. Used with appropriate component segregation [9], this method furnishes a robust technique with Laplacian interfacial tension and continuum interfacial kinematics and dynamics. A further advantage is that one can restrict computational memory requirements, such that, in 2D, for a number of immiscible components $M > 5$, computational memory requirements barely increase and execution times increase only slowly [10], [11]. Note however that generalisation of Lishchuk's method to $M > 2$ mutually immiscible components requires care if correct Laplace-Young behaviour is to emerge [12]).

All MCLB models contain an interfacial micro-current, spurious velocity or parasitic current, induced in the immediate vicinity of the fluid-fluid interface. This unphysical artefact restricts the applicability of MCLB, particularly to the continuum regime where capillary number is small. This is unfortunate since lattice Boltzmann simulation is otherwise an attractive tool for such applications. Lee and Fischer [13] and Pooley and Furtado [14] have successfully addressed the elimination of spurious flow from free-energy type MCLBs in the past. Their approaches do not, however, generalise to Lishchuk's method. The work reported here is an attempt to redress the imbalance but while we consider Lishchuk's MCLB method in particular, a large part of our analysis (i.e. sections 3, 4 and the appendices of this article) may be applied to the range of MCLB models. Shan [15] considers certain aspects of micro-current flow and sets-out generic considerations which do apply to the work reported here, as we shall see.

In section 2 we review Lishchuk's MCLB method. In section 3 we present a general analysis of external forcing in MCLB, in section 4 we treat MCLB micro-current flow in general and identify its various contributions, in section

5 we present our results and our conclusions in section 6. Throughout this article, we will use standard notation.

2 Background

In Lishchuk's MCLB method, Laplace law and 'no-traction' effects arise from a curvature-dependent external force density, impressed primarily in regions where the fluid components' phase field varies most rapidly. Let two fluid distributions occupying lattice link i, at position $\underline{r}$ be described by distribution functions, $R_i(\underline{r})$ and $B_i(\underline{r})$ (of course with $f_i(\underline{r}) = R_i(\underline{r}) + B_i(\underline{r})$). The red and blue fluids' density and their associated phase-field [9] are:

$$\rho_R = \sum_i R_i, \quad \rho_B = \sum_i B_i, \quad \rho^N = \frac{\rho_R - \rho_B}{\rho_R + \rho_B}. \tag{1}$$

Surfaces $\rho^N = constant$ define the interface with $\rho^N = 0$ its centre. Throughout the narrow but distributed interfacial region, the local interface normal is obtained from numerical approximations for the following:

$$\underline{\hat{n}} = -\frac{\underline{\nabla}\rho^N}{|\underline{\nabla}\rho^N|}. \tag{2}$$

With the above definition, for a red drop in a blue fluid, the interface normal unit vector, $\underline{\hat{n}}$ points away from the enclosed red fluid. Local interfacial curvature is obtained from the surface gradient of $\underline{\hat{n}} = (\hat{n}_x, \hat{n}_y)$, which, in two-dimensions, is [8] given by:

$$\kappa \equiv \hat{n}_x \hat{n}_y \left(\frac{\partial \hat{n}_y}{\partial x} + \frac{\partial \hat{n}_x}{\partial y} \right) - \hat{n}_y^2 \frac{\partial \hat{n}_x}{\partial x} - \hat{n}_x^2 \frac{\partial \hat{n}_y}{\partial y}. \tag{3}$$

All the derivatives in equations 2 and 3 are usually computed to $O(\underline{c}_i^4)$ accuracy with a simple, local, compact stencil:

$$\frac{\partial f}{\partial x_\alpha} = \frac{1}{k_2} \sum_{i \neq 0} t_i f(\underline{r} + \underline{c}_i) c_{i\alpha} + O(\underline{c}_i^4), \quad x_\alpha \in [x, y], \tag{4}$$

where the lattice isotropy constant $k_2 = c_s^2 = 1/3$ for the $D2Q9$ lattice used in this work. Clearly, the number of grid-points required to calculate

a gradient depends upon Q, as well as other considerations, to be discussed. Application of the normally-directed force density:

$$\underline{F} = \frac{1}{2}\sigma\kappa\underline{\nabla}\rho^N, \tag{5}$$

in which $\frac{1}{2}\underline{\nabla}\rho^N$ acts as a weight [8], may be shown to recover correct dynamics for the continuum regime [8]. That is, a Laplace Law pressure step [16] across interfacial regions and the no-traction condition arise from the force density in equation 5. Correct interfacial kinematics arise from an appropriate segregation step [17]. The kinematic property of mutual impenetrability emerges from correctly-chosen, post-collision colour segregation rules, [18], developed from the work of d'Ortona et al. [17]. We show measurement of the weighting factor in equation 5 is a key issue in the induction of micro-current activity.

The Lishchuk force is applied as an external force density to what is effectively the single fluid represented by f_i. He et al. [19] and Guo et al. [20] generalised the LBGK model originally devised by Qian et al. [24] to describe lattice fluid subject to a known, spatially variable external force density, $\underline{F}$. Collision and forcing of the distribution function (when the system is close to equilibrium, note) is:

$$f_i^{\dagger} = f_i^{(0)}\left(\rho, \rho\underline{v}\right) + \left(1 - \frac{1}{\tau}\right) f_i^{(1)}\left(\nabla\rho, ..\partial_x u_y .., \underline{F}\right) + F_i\left(\tau, \underline{F}, \underline{v}\right), \tag{6}$$

where the dagger superscript indicates a post-collision, pre-propagation quantity, $f_i^{(0)}(\rho, \underline{v})$ denotes the equilibrium distribution function [25] and the source term, F_i is [19], [20] :

$$F_i = t_i\left(1 - \frac{1}{2\tau}\right)\left(\frac{\underline{c}_i - \underline{v}}{c_s^2} + \frac{\left(\underline{c}_i.\underline{v}\right)\left(\underline{c}_i\right)}{c_s^4}\right)\cdot\underline{F}. \tag{7}$$

Here, all other symbols have their usual meaning. For a forced fluid, it is important to note that the definition of the macroscopic observables is modified:

$$\rho \equiv \sum_i f_i, \quad \underline{v} \equiv \frac{1}{\rho}\sum_i f_i\underline{c}_i + \frac{1}{2\rho}\underline{F} \tag{8}$$

Clearly, MCLB simulation relies upon the assumptions implicit in equation 6 above, most notably that the application of a fluid body force density does not drive the fluid far from its equilibrium, $f_i^{(0)}(\rho, \underline{v})$. It is very important to investigate this assumption in view of the relatively large Lishchuk

body forces required in high capillary number systems. Before proceeding with our investigation of MCLB flow artefacts therefore, we will consider this matter.

3 Analysis of external force algorithm

MCLB algorithms for simulating multi-component lattice fluid subject rely what are effectively external, immersed boundary forces applied to the lattice fluid. The problem of applying such forces was addressed by both He et al. [19] and Guo et al. [20] who take the following approximation in the force-term of the parent Bhatnagar-Gross-Krook equation [23]:

$$\underline{F} \cdot \underline{\nabla}_{\underline{\xi}} \left(f_i \right) \approx \underline{F} \cdot \underline{\nabla}_{\underline{\xi}} \left(f_i^{(0)}(\rho, \underline{v}) \right). \tag{9}$$

The interfacial micro-current is an error which is most acute when Ca is small i.e. for relatively large immersed boundary force. Clearly, when considering the origin of the micro-current, it is necessary to confirm that, at typical parameterisations, the lattice fluid is not forced so far from equilibrium that the approximation in equation 9 is violated. Here we derive an approximate expression for the change in f_i due to an immersed boundary Lishchuk–type force [8], in terms of the macroscopic lattice fluid viscosity, $\nu(\tau)$, interfacial tension, σ, interfacial width parameter β, etc., and from it obtain an appropriate condition.

Consider a $D2Q9$ lattice. Neglect the effects of curvature except in the source term of the evolution equation. Let the local interface be orientated perpendicular to the x-direction and centred on $x = 0$ within a two-dimensional lattice fluid of uniform viscosity $\nu(\tau)$. Neglecting flow ($\underline{v} = \underline{0} \iff f_i^{(0)}(\rho, \underline{0}) = t_i \rho(x), F_i = t_i \frac{1}{c_s^2} \left(1 - \frac{1}{2\tau}\right) \left(\underline{F} \cdot \underline{c_i}\right)$ [20]) and density variation in the direction perpendicular to x and taking the steady-state of the LBGK evolution equation, the distribution function is governed by difference equations obtained from equation 6:

$$f_i(x+c_{ix}) = f_i(x) + \frac{1}{\tau} \left(t_i \rho(x) - f_i(x) \right) + t_i \left(1 - \frac{1}{2\tau}\right) \frac{F(x) c_{ix}}{c_s^2}, \quad i = 0..8, \tag{10}$$

where $c_{ix} = \pm 1, 0$ for the D2Q9 lattice. Here $F(x)$ is the macroscopic, external, immersed boundary or Lishchuk force. In the present case, we will neglect its component parallel to the local interface. Exclude $c_{ix} = 0$

(we return to this case) and expand about x in equation 10, then use an integrating factor:

$$\begin{aligned} f_i(x) &= \exp\left(-\frac{x}{c_{ix}\tau}\right) \\ &\times \left(\int^x \frac{t_i}{c_{ix}}\left(\frac{\rho(u)}{\tau}+\left(1-\frac{1}{2\tau}\right)\frac{F(u)c_{xi}}{c_s^2}\right)\exp\left(\frac{u}{c_{ix}\tau}\right)du + C_0\right), \end{aligned} \tag{11}$$

where C_0 is a constant.

Now, in hydrostatic equilibrium the density and external force are related by the x-component of the weakly compressible Navier-Stokes equation as $\frac{1}{c_s^2}\frac{d\rho}{dx} = F(x)$, with $F(x) = \frac{\sigma\kappa}{2}\frac{d\rho^N}{dx}$ [8], hence:

$$\rho(x) = \frac{1}{c_s^2}\int_{-\infty}^{x} F(u)du + \rho(-\infty) = \frac{\kappa\sigma}{2c_s^2}\rho^N(x) + \rho(-\infty). \tag{12}$$

Here $\rho^N(x)$ is the interfacial phase field. With the present approximations, $\rho^N(x)$ and the associated meso-scale force are given by [12]:

$$\rho^N(x) = \tanh(\beta x), \quad F(x) = \frac{1}{2}\kappa\sigma\beta\left(1-\tanh^2(\beta x)\right), \tag{13}$$

where β is the colour segregation parameter, which controls the width of the interfacial region $W \sim \frac{1}{\beta}$ and the factor $\frac{1}{2}$ arises as a normalisation constant [8]. Substituting equations 12 and 13 into equation 11 it is possible to write down an explicit integral for $f_i(x)$. This integral is difficult, so we take the following approximate form for the magnitude of the Lishchuk force given in equation 13:

$$F(x) = \begin{cases} \frac{1}{2}\kappa\sigma\beta\left(\frac{W^2-x^2}{W^2}\right) & |x| \le W, \\ 0 & |x| > W. \end{cases} \tag{14}$$

The corresponding density is obtained using equation 12:

$$\rho(x) = \begin{cases} \rho(-\infty) & x < -W, \\ \frac{\kappa\sigma\beta}{6c_s^2W^2}(3W^2x - x^3 + 2W^3) + \rho(-\infty) & |x| \le W, \\ \frac{2\kappa\sigma\beta W}{3c_s^2} + \rho(-\infty) & x > W. \end{cases} \tag{15}$$

Here W may be used to match the width of the forced region to that implicit in equation 13. Substituting approximations 14 and 15 into equation 11 the

integration may be performed. For $x < -W$ we obtain $f_i(x) = t_i\rho(\infty) + C_1 \exp\left(-\frac{x}{c_{ix}\tau}\right)$, in which, for $x < -W, c_{ix} > 0$, the exponential contribution is seen to be unbounded. Hence $C_1 = 0$. Similar arguments may be applied to to the case of $x > W$:

$$f_i(x) = t_i\rho(x), \quad |x| > W. \tag{16}$$

For $|x| \leq W$, after repeated application of integration by parts followed by elimination of variables in the resulting expression:

$$\begin{aligned} f_i &= t_i\rho(x) \\ &+ \frac{\kappa\sigma\beta c_{ix}\tau}{2W^2c_s^2} t_i \left(c_{ix} - \frac{c_{ix}}{2\tau} - 1\right)\left(W^2 - x^2 + 2c_{ix}\tau x - 2\tau^2 c_{ix}^2\right) \\ &+ C_2 \exp\left(-\frac{x}{\tau c_{ix}}\right), \qquad |x| < W, \end{aligned} \tag{17}$$

where C_2 is an integration constant. $C_2 = 0$ by considering the case of W large. Hence:

$$\begin{aligned} f_i(x) \equiv G_i(x) &= t_i\rho(x) \\ &+ \frac{\kappa\sigma\beta c_{ix}\tau}{2W^2c_s^2} t_i \left(c_{ix} - \frac{c_{ix}}{2\tau} - 1\right) \\ &\times \left(W^2 - x^2 + 2c_{ix}\tau x - 2\tau^2 c_{ix}^2\right), \quad |x| < W. \end{aligned} \tag{18}$$

The rest equilibrium in the Lishchuk-LBGK-Guo model is $f_i^{(0)} = t_i\rho(x)$, so $f_i^{(1)}(x) = f_i(x) - t_i\rho(x)$, so we arrive at the following estimate of the relative departure from its equilibrium of the distribution function in an externally-forced fluid:

$$\frac{f_i^{(1)}(x)}{f_i^{(0)}(x)} = \begin{cases} 0 & x < -W, \\ G_i(x) & |x| \leq W, \\ 0 & x > W, \end{cases} \tag{19}$$

where $G_i(x)$ is defined in equation 18. Note $\frac{f_i^{(1)}(x)}{f^{(0)}(x)}$ is discontinuous at the boundaries of the forced region $x = \pm W$, corresponding to the discontinuity in the assumed force.

Now, we have already assumed $c_{ix} \neq 0$. Recall also $\tau \in [0.5, \infty)$. Consider equation 19 in two limits. For large τ $\left|\frac{f_i^{(1)}(x)}{f_i^{(0)}(x)}\right| \leq \frac{\kappa\sigma\beta\tau^3}{2W^2c_s^2\rho(x)}$, for small $\tau \in$

$[0.5, \frac{W}{c_{ix}})$ a stationary value occurs at $x = c_{ix}\tau$ and $c_{ix} = -1$ gives the upper bound of $\left|\frac{f_i^{(1)}(x)}{f_i^{(0)}(x)}\right| \leq \frac{\kappa\sigma\beta}{2W^2c_s^2\rho(x)}\left(W^2 - \tau^2\right)\left(2\tau - \frac{1}{2}\right)$. For a typical interface with $W = 3$ and small $\tau \in [0.5, \frac{W}{c_{ix}})$ the last condition reduces to $\left|\frac{f_i^{(1)}(x)}{f_i^{(0)}(x)}\right| \leq \frac{\kappa\sigma\beta}{5c_s^2\rho(x)}$. In summary, we arrive at the following condition for the validity of the approximations implicit a Lishchuk-type immersed boundary method, based upon He et al. [19] and Guo et al., [20]:

$$\frac{\kappa\sigma\beta}{c_s^2\rho} \ll 1. \tag{20}$$

We pause to consider equation 20 in the context of other MCLB models. The preceding analysis applies to lattice fluid subject to an immersed boundary type body force, $\mathbf{F}$. It is facilitated by the fact that structure of the phase field ρ^N is known in Lishchuk's model. Li et al. [21] showed that it is possible to formulate the Shan-Chen (SC) and Exact Difference MCLB [22] methods in terms of a body force. In the case of SC (probably the most widely-used MCLB), Li et al. derive equilibria and source terms, F_i, with identical structure to those we have assumed. Hence, an analysis similar to that culminating in equation 20 above may, in principle, be applied to the SC MCLB method, with $\underline{F} \approx -G\pi\underline{\nabla}\phi$, once the structure of the interface density profile is deduced, for some value of temperature-like parameter, G [7] and a choice of function ϕ. (This traditional notation for the SC thermodynamic parameter, ψ, should not be confused with the Stokes stream-function we us elsewhere.) For thermodynamic consistency, $\psi = e^{-\frac{1}{\rho}}$ yields a result which might be modelled in a manner similar to that applied here.

A calculation based upon the exact interfacial profile defined in equation 13, performed in the same steps as those set-out above yields the following replacement for equation 18:

$$\begin{aligned} f_i(x) &= t_i\rho(-\infty) \\ &+ \frac{\kappa\sigma}{2c_s^2}t_i\left(1 - \frac{1}{2\tau}\right)\tanh(\beta x) \\ &- \frac{\kappa\sigma}{4c_s^2\tau}t_{i2}F_1\left(1, \gamma : 1 + \gamma : -e^{2\beta x}\right) \\ &- \frac{\kappa\sigma}{4c_s^2\tau}t_i\left(\frac{e^{2\beta x}}{1 + \beta c_{ix}\tau}\right){}_2F_1(1, 1 + \gamma; 2 + \gamma; -e^{2\beta x}), \end{aligned} \tag{21}$$

where $\gamma = \frac{1}{2\beta c_{ix}\tau}$. This result may be simplified to $x = 0$ i.e. the centre of the interface in which case ${}_sF_1(1, a; 1 + a; -1) = \frac{a}{2}\left(\psi\left(\frac{a+1}{2}\right) - \psi\left(\frac{a}{2}\right)\right)$ where ψ denotes the digamma function. Under these circumstances the values of the hypergeometric functions ${}_2F_1$ are of of order unity and are omitted. Now condition 20 becomes $\frac{\kappa\sigma\beta}{c_s^2\rho}\left|\frac{c_{ix}}{1+2c_{ix}\tau\beta}\right| < 1$.

Let us consider the case $c_{ix} = 0$ and off-lattice links perpendicular to the direction of the force, when it is immediate from equation 10 that $f_i^{(1)}(x) = 0, \forall x$.

4 Analysis of micro-current flow

Micro-current flow should be treated as a low Re flow of compressible fluid, since density variation may be significant in the interfacial region. We therefore begin with the compressible formulation of flow. Here we take the origin to coincide with the centre of a red drop immersed in a blue fluid, so that $\rho^N(\underline{0}) = 1$. The macroscopic dynamics of a compressible, two-dimensional lattice fluid in the steady, low Re limits, subject to Lishchuk's interfacial force, is described by the following system of coupled, linear partial differential equations [8], [16]:

$$\underline{V} - c_s^2\underline{\nabla}\rho + \underline{F} = \underline{0}, \quad \underline{\nabla}\cdot(\rho\underline{v}) = 0, \quad \underline{F} = \frac{1}{2}\sigma\kappa\underline{\nabla}\rho^N, \tag{22}$$

in which the dissipation vector components may be written in suffix notation $V_\alpha \equiv \nu(\tau)\frac{\partial}{\partial x_\beta}(2\rho S_{\alpha\beta})$, $\alpha \in [1, 2]$ (see below). Here $S_{\alpha\beta}$ is the symmetric velocity gradient tensor.

We expand the velocity, density and force fields about a base state of rest:

$$\underline{F} = \frac{\kappa_0\sigma}{2}\underline{\nabla}\rho^N + \underline{\delta F}, \quad \underline{v} = \underline{\delta v}, \quad V_\alpha = \delta V_\alpha, \quad \rho = \rho_0 + \delta\rho. \tag{23}$$

Here κ_0 is a local average curvature which is taken to be constant. Force fluctuation $\underline{\delta F}$ is responsible for driving the interfacial micro-current, $\underline{\delta v}$ and its associated density adjustment, $\delta\rho$. $\underline{\delta F}$ arises from identified numerical errors $\underline{\delta F} = \sum_{j=1}^{3}\underline{\delta F}^{(j)}$. Term $j = 1$ arises in evaluation of first partial derivatives, $j = 2$ arises as discussed below and $j = 3$ arises from numerical error in the measurement of κ i.e. second partial derivatives. Each term produces an associated velocity, dissipation and density adjustment:

$$\underline{\delta F} \;=\; \underline{\delta F}^{(1)} + \underline{\delta F}^{(2)} + \underline{\delta F}^{(3)}, \tag{24}$$

$$
\begin{aligned}
\underline{\delta v} &= \underline{\delta v}^{(1)} + \underline{\delta v}^{(2)} + \underline{\delta v}^{(3)}, \\
\underline{\delta V} &= \underline{\delta V}^{(1)} + \underline{\delta V}^{(2)} + \underline{\delta V}^{(3)}, \\
\delta\rho &= \delta\rho^{(1)} + \delta\rho^{(2)} + \delta\rho^{(3)}.
\end{aligned}
$$

It is possible to separate the flow responses in equations 24 in this way because the underlying description is linear. Substituting equations 23 and 24 into equations 22 we separate contributions:

$$
\begin{aligned}
\underline{\delta V}^{(j)} - c_s^2 \underline{\nabla}\left(\delta\rho^{(j)}\right) + \underline{\delta F}^{(j)} &= \underline{0}, \quad j \in [1..3], \\
\underline{\nabla}\cdot\left(\rho_0 \underline{\delta v}^{(j)}\right) &= 0, \quad j \in [1..3], \\
\underline{\nabla}\left(c_s^2\rho_0 - \frac{1}{2}\kappa_0\sigma\rho^N\right) &= \underline{0},
\end{aligned}
\tag{25}
$$

We show in the appendices (section B) that one can find a materially conserved scalar analogous to Stokes' stream-function, which is used to represent the micro-current flow described by the above system.

Viscous dissipation means flow vanishes in the absence of driving force:

$$
\underline{\delta F}^{(j)} = \underline{0} \iff \underline{V}^{(j)} = \underline{0}, \quad \underline{\nabla}(\delta\rho^{(j)}) = \underline{0}. \tag{26}
$$

That is, by eliminating an error force contribution $\underline{\delta F}^{(j)} = \underline{0}$, we expect to eliminate the corresponding micro-current and density fluctuations $\underline{\delta v}^{(j)}$, $\delta\rho^{(j)}$. Deferring consideration of the effects of $\underline{\delta F}^{(3)}$ until section 5, we seek to achieve this in the next section by finding $\underline{\delta F}^{(j)}, j \in [1,2]$, then adding its negative into the Lishchuk force. Note that the dissipation is now given as:

$$
\delta V_\alpha^{(j)} = \nu(\tau)\frac{\partial}{\partial x_\beta}\left(2\rho_0\delta S_{\alpha\beta}^{(j)}\right), \quad \delta S_{\alpha\beta}^{(j)} = \frac{1}{2}\left(\frac{\partial\delta v_\alpha^{(j)}}{\partial x_\beta} + \frac{\partial\delta v_\beta^{(j)}}{\partial x_\alpha}\right), \tag{27}
$$

and that (from the third of equations 25) the base state of density is $\rho_0(\underline{r}) = \rho_0(0) + \frac{\kappa_0\sigma}{2c_s^2}\left(\rho^N(\underline{r}) + 1\right)$. From the first of equations 25, using standard properties of the vector field:

$$
\begin{aligned}
\underline{\nabla}\times\underline{\delta F}^{(j)} &= -\underline{\nabla}\times\left(\underline{\delta V}^{(j)}\right), \\
\underline{\nabla}\cdot\underline{\delta F}^{(j)} &= c_s^2\nabla^2\delta\rho^{(j)} - \underline{\nabla}\cdot\left(\underline{\delta V}^{(j)}\right).
\end{aligned}
\tag{28}
$$

Measurements show that the divergence of the dissipation vector $\delta\underline{V}^{(j)}$ at least two orders of magnitude smaller than $\nabla^2\delta\rho^{(j)}$. Hence, we see that to a good approximation, the divergence of the error force $\underline{\delta F}^{(j)}$ determines the density adjustment $\delta\rho^{(j)}$ while the interfacial micro-current is the system's adjustment to the rotational part.

4.1 Micro-current Contributions

Error in the applied external force arises from two sources. First, anisotropic stencil contributions (originally identified by Shan [15]) are contained in our error force $\underline{\delta F}^{(1)}$. These produce the tangential force at the interface [15] considered in section 4.2. A second contribution $\underline{\delta F}^{(2)}$ arises when accumulating samples of the continuous immersed boundary force. Both must have the symmetry of the underlying lattice. Recall, micro-current velocity (compressible Stokes stream-function) induced by $\underline{\delta F}^{(j)}$ is denoted $\underline{\delta v}^{(j)}$ ($\psi^{(j)}$) and these contributions superpose. Each may, in principle, be eliminated. Vector fields $\underline{\delta v}^{(1)}$ and $\underline{\delta v}^{(2)}$ appear to be linearly independent i.e. no stencil considered here is capable of producing a flow response $\underline{\delta v}^{(1)}$ such that:

$$\underline{\delta v}^{(1)}(\underline{r}) = -\underline{\delta v}^{(2)}(\underline{r}), \quad \forall \underline{r}, \tag{29}$$

(see section 5) though the tantalising possibility of such a cancellation cannot be ruled-out.

4.2 Response to Choice of Stencil

We consider the measurement of interface force on a lattice. For simplicity take an ideal, circular phase field of constant curvature with an interface force derived from its gradient:

$$\rho^N(r,\phi) = \tanh\left(\beta(r-R_0)\right), \quad \underline{F}^{(1)}(r,\phi) = \frac{1}{2}\frac{\sigma}{R_0}\underline{\nabla}\rho^N. \tag{30}$$

$\underline{\nabla}\rho^N$ will be evaluated using a variety of stencils in this section. In section 5 we consider a fully coupled phase field and curvature measurement effects.

Shan [15] showed that anisotropic terms in a stencil generate micro-current flow. To quantify this observation, we construct stencils for the evaluation, on a lattice, of approximations from which different anisotropic

terms are eliminated. Taking a Taylor expansion about $\underline{r}$, of the quantity $t_i\theta(\underline{r}+\underline{c}_i)c_{ix}$ and summing on i:

$$\begin{aligned} k_2\frac{\partial\theta}{\partial x} &= \sum_i t_i\theta(\underline{r}+\underline{c}_i)c_{ix} \\ &- \sum_{n=2}^{\infty}\frac{1}{(2n-1)!}T\left(2n,\{\underline{c}_i,i=1..Q\}\right)_{x,\alpha_1,\alpha_2\ldots\alpha_{2n-1}} \\ &\times \frac{\partial}{\partial x_{\alpha_1}}\frac{\partial}{\partial x_{\alpha_2}}\ldots\frac{\partial\theta}{\partial x_{\alpha_{2n-1}}}, \end{aligned} \tag{31}$$

where $\alpha_k, x_{\alpha_k}\in[x,y]$ and:

$$T\left(n,\{\underline{c}_i,i=1..Q\}\right)_{\alpha_1\alpha_2\ldots\alpha_n}\equiv\sum_{i=1}^{Q}t_ic_{i\alpha_1}c_{i\alpha_2}\ldots c_{i\alpha_n}, \tag{32}$$

are the lattice tensors' components. Odd-order lattice tensors vanish, note. For the $D2Q9$ lattice, only the second and fourth order tensors are isotropic. Expressions for higher-order tensors are constructed by straightforward linear algebra techniques as sums of products of lower-order tensors:

$$\begin{aligned} \sum_{i=1}^{Q}t_ic_{i\alpha_i}c_{i\alpha_j} &= k_2\delta_{ij}, \\ \sum_{i=1}^{Q}t_ic_{i\alpha_i}c_{i\alpha_j}c_{i\alpha_k}c_{i\alpha_l} &= \Delta_{ijkl}=k_4\left(\delta_{ij}\delta_{kl}+\delta_{ik}\delta_{jl}+\delta_{il}\delta_{jk}\right), \\ \sum_{i=1}^{Q}t_ic_{i\alpha_i}c_{i\alpha_j}c_{i\alpha_k}c_{i\alpha_l}c_{i\alpha_m}c_{i\alpha_n} &= k_4\left(\delta_{ij}\Delta_{klmn}+\ldots-2\delta_{ijklmn}\right), \end{aligned} \tag{33}$$

where the ellipsis $\delta_{ij}\Delta_{klmn}+\ldots$ denotes the sum of $\frac{5\times6}{2}$ terms generated by permutation of subscripts. It is immediate from equation 32 that lattice tensors have the property:

$$T\left(n,\{z\underline{c}_i,i=1..Q\}\right)_{\alpha_1\alpha_2\ldots\alpha_n}=z^nT\left(n,\{\underline{c}_i,i=1..Q\}\right)_{\alpha_1\alpha_2\ldots\alpha_n}. \tag{34}$$

In equation 31 the leading error (though not the most significant) has $n=2$ and is $O(c^4)$:

$$\epsilon^{(4)}\left(\frac{\partial\psi}{\partial x}\right)=\frac{1}{3!k_2}\sum_{i=1}^{Q}t_ic_{i\alpha_1}c_{i\alpha_2}c_{i\alpha_3}c_{ix}\frac{\partial}{\partial x_{\alpha_1}}\frac{\partial}{\partial x_{\alpha_2}}\frac{\partial\psi}{\partial x_{\alpha_3}}. \tag{35}$$

The isotropy conditions (equation 31) may be used to show:

$$\epsilon^{(4)}\left(\underline{\nabla}\theta\right) = \frac{1}{2}\frac{k_4}{k_2}\nabla^2\left(\underline{\nabla}\theta\right), \tag{36}$$

which, for circular symmetry $\theta = \theta(r)$, gives for the leading error associated with the gradient as $\epsilon^{(4)}\left(\underline{\nabla}\theta\right) = \frac{1}{2}\frac{k_4}{k_2}\left(\frac{\partial^2\theta}{\partial r^3} - \frac{1}{r^2}\frac{\partial\theta}{\partial r}\right)\hat{e}_r$. We show below that such an irrotational force excites a relatively weak micro-current but a stronger density perturbation. To obtain the $O(6)$ error term in the gradient, use the third of equations 33 and some algebra:

$$\epsilon^{(6)}\left(\underline{\nabla}\theta\right) = \frac{1}{5!}\frac{k_4^2}{k_2}\nabla^2\nabla^2\underline{\nabla}\theta - \frac{2}{5!}\frac{k_4}{k_2}\left(\frac{\partial^5\theta}{\partial x^5}, \frac{\partial^5\theta}{\partial y^5}\right), \tag{37}$$

which clearly has a rotational part $\frac{2}{5!}\frac{k_4}{k_2}\frac{\partial^2\theta}{\partial x\partial y}\left(\frac{\partial^4\theta}{\partial x^4} - \frac{\partial^4\theta}{\partial y^4}\right)$, which will be non-zero, even for $\theta = \theta(r)$ axially symmetric.

We develop practical stencils for measuring lattice gradient from which anisotropic terms $\epsilon^{(n)}$, $n \geq 6$ are preferentially eliminated, using equations 31 and 34. That defined below (which is not compact, note) refers to the a_n in table 1:

$$\frac{\partial\theta}{\partial x} \approx \sum_{n=1}^{N} a_n \sum_{i=1}^{Q} t_i\theta(\underline{r} + n\underline{c}_i)c_{ix}. \tag{38}$$

For example, using table 1 stencil $A_{6,4}$, which eliminates $\epsilon^{(6)}$ (only), gives the following approximation:

$$\frac{\partial\theta}{\partial x} = \sum_i t_i\left(3.2\theta(\underline{r} + \underline{c}_i) - 0.1\theta(\underline{r} + 2\underline{c}_i)\right)c_{ix} + O(\epsilon^{(4)}) + O(\epsilon^{(8)}). \tag{39}$$

In comparison $A_{6,*}$ from which only the isotropic error $\epsilon^{(4)}$ has been eliminated is $\frac{\partial\theta}{\partial x} = \sum_i t_i\left(4\theta(\underline{r} + \underline{c}_i) - 0.5\theta(\underline{r} + 2\underline{c}_i)\right)c_{ix} + O(\epsilon^{(6)})$. The computational overhead of a particular stencil is proportional to its number of non-zero a_n. Consider table 1 and figure 5. The micro-current activity associated with a stencil we quantify by the maximum of the absolute value of the rectangular compressible Stokes stream-function (see appendix B). Comparing the performance of equally-expensive stencils $A_{6,*}$ and $A_{8,4}$ (rows 2, 3) we infer that eliminating $\epsilon^{(4)}$ is not as beneficial as eliminating anisotropic contributions associated with $\epsilon^{(6)}$. Put another way, the overhead of stencils $A_{6,*}$ and $A_{8,4}$ is identical but the performance of the latter is superior,

despite its lower formal level of formal accuracy. In line with Shan's observations [15], the performance of more elaborate stencils $A_{10,4}$, $A_{12,4}$ etc. (rows 4,5) saturate. The data in lines 3-5 of table 1 support the observation that while the micro-current contribution associated with the stencil, $\underline{\delta v}^{(1)}$, is removed almost completely by what we designate optimally efficient stencil $A_{8,4}$, there remains the small, independent contribution $\underline{\delta v}^{(2)}$ (which has a different structure, note) associated with sampling. We shall consider this contribution in the next section and postpone further consideration of contribution $\underline{\delta v}^{(1)}$ until section 5.

Table 1: Designation, defining numerical coefficients and performance for the stencils in equation 38 which approximate $\frac{\partial \psi}{\partial x}$. The value of n (m) indicates the lowest order of what we designate the anisotropic (isotropic) terms of the stencil. The a_ns tabulated here relate to the $D2Q9$ Lattice. Only stencil $A_{6,4}$ is compact, note. The maximum value of the induced micro-current's compressible rectangular Stokes stream-function for each stencil is used to quantify performance with a smaller value of the latter indicative of superior performance.

Name	n	m	a_1	a_2	a_3	a_4	$\max(\lvert\psi^1 + \psi^2\rvert)$
$A_{6,4}$	6	4	3.0	0	0	0	0.11
$A_{6,*}$	6	$*$	4.0	0.5	0	0	0.43
$A_{8,4}$	8	4	3.2	-0.1	0	0	0.027
$A_{10,4}$	10	4	3.31	-0.17	0.01	0	0.028
$A_{12,4}$	12	4	3.37	-0.21	0.02	-0.001	0.027

4.3 Response to Idealised Force Distribution

The micro-current, force and density fluctuation associated with this sampling error considered in this section are denoted $\underline{\delta v}^{(2)}$, $\delta\rho^{(2)}$ and $\underline{\delta F}^{(2)}$. To expose artefacts which arise solely as a result of using a sampled but otherwise exact Lishchuk force, we consider a two-dimensional lattice fluid subject to a force distribution derived from an idealised phase field of curvature R, where:

$$\begin{aligned} \rho^N(r,\phi) &= \tanh\left(\beta(r-R)\right), \\ F_r^{(2)}(r,\phi) &= \beta\left(1-\rho^{N2}(r,\phi)\right), \quad F_\phi^{(2)}(r,\phi) = 0. \end{aligned} \tag{40}$$

Expand the second of equations 25:

$$\rho_0 \frac{\partial \delta v_\beta^{(2)}}{\partial x_\beta} + \delta v_\beta^{(2)} \frac{\partial \rho_0}{\partial x_\beta} = 0, \tag{41}$$

For an idealised force distribution, the tangential micro-current flow is confined to the interfacial region (see figure e.g figure 3) i.e. to have a spatial scale W. Hence, we obtain from equation 41 the estimates balance:

$$\rho_0 \frac{\delta v^{(2)}}{W} \approx \delta v^{(2)} \frac{\sigma\kappa}{c_s^2 W}. \tag{42}$$

Here δv is an estimate of the micro-current velocity and we estimated the density variation from the Laplace pressure step. Clearly the first set of terms in the left hand side of equation 41 will be small compared with the second provided:

$$\frac{\left(\rho_0 \frac{\delta v^{(2)}}{W}\right)}{\left(\delta v^{(2)} \frac{\sigma\kappa}{c_s^2 W}\right)} = \frac{\rho_0 c_s^2}{\sigma\kappa} \ll 1. \tag{43}$$

Hence, provided the density step across the interfacial region is small compared with the average density ($\sim \rho_0$), continuity equation 41 reduces to the incompressible form $\underline{\nabla} \cdot \underline{\delta v}^{(2)} = 0$. With this simplification the first of equations 25 becomes:

$$\nu(\omega)\rho_0 \nabla^2 \delta v_\alpha^{(2)} + 2\nu(\omega)\delta S_{\alpha\beta}^{(2)} \frac{\partial \rho_0}{\partial x_\beta} - c_s^2 \frac{\partial \delta\rho^{(2)}}{\partial x_\alpha} + \delta F_\alpha^{(2)} = 0. \tag{44}$$

The ratio of the first to the second term in the above is large:

$$\frac{\left(\nu(\omega)\rho_0 \frac{\delta v^{(2)}}{W^2}\right)}{\left(\nu(\omega)\frac{\delta\rho\delta v^{(2)}}{W^2}\right)} = \frac{\rho_0}{\delta\rho} \gg 1, \tag{45}$$

and taking the curl to eliminate the density fluctuation $\delta\rho^{(2)}$ in equation 44, we find the following equation for the two-dimensional micro-current due to an idealised immersed boundary force:

$$\nu(\omega)\nabla^2 \underline{\nabla} \times \underline{\delta v}^{(2)} + \underline{\nabla} \times \underline{\delta F}^{(2)} \approx \underline{0}. \tag{46}$$

Taking the divergence of equation 44 and noting that the divergence of the dissipation is measured to be $O(10^{-5})$ smaller than $|\underline{\nabla}\rho^{(2)}|$ we also find:

$$c_s^2\nabla^2\delta\rho^{(2)} - \underline{\nabla}\cdot\underline{\delta F}^{(2)} \approx 0. \tag{47}$$

The importance of the force term in equation 46 becomes clear when we seek $\underline{\delta v}^{(2)}$ from its associated steam-function, by solving $\nabla^2\nabla^2\psi^{(2)} = 0$ whilst applying Von Neumann boundary conditions which attempt to model the effects of $\underline{\delta F}^{(2)}$. We investigate this matter more fully in appendix A, where it is shown that micro-current flow patterns calculated in this way exhibit limited agreement with those observed in fluids subject to the idealised force distribution defined in equations 30. We therefore conclude that the spatial variation of the force fluctuation $\underline{\delta F}^{(2)}(\underline{r})$ is significant and that it is necessary to continue with a description based upon equation 46.

Now, using cylindrical polar co-ordinates, we write:

$$\begin{aligned}
\underline{\nabla}\times\underline{\delta F}^{(2)} &= \left(\frac{1}{r}\frac{\partial}{\partial r}(r\delta F_\phi^{(2)}) - \frac{1}{r}\frac{\partial}{\partial\phi}\delta F_r^{(2)}\right)\hat{e}_z = -\frac{1}{r}\frac{\partial\delta F_r^{(2)}}{\partial\phi}\hat{e}_z, \qquad (48)\\
\underline{\nabla}\cdot\underline{\delta F}^{(2)} &= \frac{1}{r}\frac{\partial}{\partial r}(r\delta F_r^{(2)}) + \frac{1}{r}\frac{\partial}{\partial\phi}\delta F_\phi^{(2)} = \frac{1}{r}\frac{\partial\delta F_r^{(2)}}{\partial r},\\
\nabla^2\delta\rho^{(2)} &= \frac{1}{r}\left(\frac{\partial}{\partial r}\left(r\frac{\partial}{\partial r}\delta\rho^{(2)}\right)\right) + \frac{1}{r^2}\frac{\partial^2}{\partial\phi^2}\delta\rho^{(2)}\\
&\approx \frac{1}{r}\left(\frac{\partial}{\partial r}\left(r\frac{\partial\delta\rho^{(2)}}{\partial r}\right)\right),
\end{aligned}$$

since $\underline{F}^{(2)}$ is purely radial by assumption, and $\delta\rho^{(2)}$ is dominated by its radial variation, see figure 1. Consider first equation 46. Figure 1 shows the dissipation field measured from the micro-current in a simulation of lattice fluid with $\omega = 1.3$, subject to the force distribution of equation 30 with $R = 45$ (solid lines indicate the location of the interface centre), together with its curl. The structure of the latter suggests a separable form for the rotational part of the micro-current dissipation i.e. for $\nu(\omega)\nabla^2\underline{\nabla}\times\underline{\delta v}^{(2)}$ which conforms with the underlying lattice symmetry:

$$\nu(\omega)\nabla^2\underline{\nabla}\times\underline{\delta v}^{(2)} = \left(\frac{f(\rho^N)\sin(4\phi)}{R}\right)\hat{e}_z, \tag{49}$$

where ϕ may be interpreted as the polar angle of the interfacial normal or colour field, r may be interpreted as radial distance from the centre of curvature and the radial structure of dissipation is related to $\rho^N(r)$ for convenience.

We discuss these issues shortly. Hence, from equations 46, 48 and 49:

$$\delta F_r^{(2)} = \frac{r}{4R} f(\rho^N)\cos(4\phi) + g(r), \tag{50}$$

where $g(r)$ is an undetermined function of r (recall, $\underline{\nabla} \times \underline{a} = \underline{\nabla} \times (\underline{a} + \underline{\nabla}\xi)$). Now, consider first equation 47. Figure 1 shows the variations of $\delta\rho^{(2)}$. For this data, we measure $\max\left(\frac{1}{\delta\rho^{(2)}}\frac{\partial\delta\rho^{(2)}}{\partial\phi}\right) < 0.11$. Accordingly, we neglect the dependence upon ϕ of $\delta\rho^{(2)}$. From equations 47 and 48, we obtain $r\delta F_r^{(2)} = c_s^2\frac{\partial}{\partial r} r\delta\rho^{(2)} + h(\phi)$. Neglecting the r variation in the right hand side and relaxing the result to compensate for this, we have $\delta F_r^{(2)} = c_s^2\frac{\partial\delta\rho^{(2)}}{\partial r} + h(r,\phi)$ which is consistent with equation 50 provided $h(r,\phi) = \frac{r}{4R} f(\rho^N)\cos(4\phi)$, $g(r) = c_s^2\frac{\partial\delta\rho^{(2)}}{\partial r}$, hence:

$$\delta F_r^{(2)} = \frac{r}{4R} f(\rho^N)\cos(4\phi) + c_s^2\frac{\partial\delta\rho^{(2)}}{\partial r}, \quad \delta F_\phi^{(2)} = 0, \tag{51}$$

It is convenient to relate the radial structure to ρ^N. In figure 2 the discrete data in the upper two plots corresponds to the lattice-value of the curl of the same two-dimensional micro-current dissipation field, now plotted against ρ^N, for all the lattice points within the angular interval $[0, \frac{\pi}{4}]$, with stated values of interface width parameter, β. Note that the continuum interface location corresponds to $\rho^N = 0$ and that the density of data points increases as $|\rho^N| \to 1$, since there are more lattice points located in the bulk. The continuous lines in the first and second of figures 2 are the following empirical fits:

$$\begin{aligned}
f(\beta,\rho^N) &= c^\beta\left(\sum_{n=1}^{N} a_n^\beta\left(\rho^N\right)^n\right)\exp\left(b^\beta(\rho^N)^2\right), \qquad (52)\\
\underline{a}^{0.3} &= (0.45, -0.20, -1.60, 0.29, 0.61, -0.09)\,,\\
b^{0.3} &= 2.0,\\
c^{0.3} &= H(\rho^N + 0.978) - H(\rho^N - 0.978),\\
\underline{a}^{0.6} &= (0.23, 0.0, -0.55, 0.0, 0.42, 0.0, -0.10, 0.0)\,,\\
b^{0.6} &= 3.0,\\
c^{0.6} &= 1.0,
\end{aligned}$$

in which the polynomial (exponential) factor has been used to impose the nodal structure (amplitude ratio). In figure 2 the data in the lower plot

shows the dependance of the maximum value of dissipation upon the radius of curvature of the interfacial region, R. Note that $\rho^N < 0$ corresponds to the exterior fluid. Clearly, the qualitative structure of the near-interfacial circulation is affected by the value of β, at given R. This is to be expected considering the origin of error force $\underline{\delta F}^{(2)}$- for larger β i.e. a narrower interface, the error associated with sampling the Lishchuk force must increase. Also to be expected is the fact that this data exhibits similar levels of flow structure over similar ranges of phase field, ρ^N. Clearly however, the corresponding spatial range for the case of $\beta = 0.3$ is greater than that for $\beta = 0.6$. The estimate of dissipation for $\beta = 0.3$ is therefore superior to that for $\beta = 0.6$. Numerical derivatives are required to estimate dissipation and those issues with numerical derivatives already discussed mean that we chose stencil $A_{8,4}$. Clearly the fits above are subject to certain considerations. For $\beta = 0.6$ we have chosen to use an odd order polynomial with symmetrically distributed approximate roots. Here one pair is located at $\rho^N \approx \pm 1$ to ensure that modelled activity diminishes in the bulk components. For $\beta = 0.3$ roots close to $\rho^N = \pm 1$ are neglected necessitating the use of the cut-off defined above.

In summary, we find that the micro-current-inducing, purely radial error $\underline{\delta F}^{(2)}$ due solely to the effect of sampling an exact Lishchuk interface force is balanced mainly by the gradient in the density adjustment, $\delta\rho^{(2)}$. However, a radial force can also produce the predominantly tangential flow response if we recall that it is the micro-current dissipation, $\underline{V}$ which is related to $\underline{\delta F}^{(2)}$ and not $\underline{\delta v}^{(2)}$ itself, see equation 46. It is the first term in equation 51 which is effective against the second identified micro-current contribution discussed in this section. We postpone further discussion until section 5.

5 Results and Discussion

First consider that numerical error associated with anisotropic contributions to the stencil used to determine the interface force. By preferentially eliminating anisotropic contributions to the stencil, $\epsilon^{(2n)}$ $n \geq 3$, we may more efficiently reduce the micro-current $\underline{\delta v}^{(1)}$ (see table 1 above). Figure 5 compares the result on the measured response $\psi^1 + \psi^2$ of removing different error terms $\epsilon^{(2n)}$ from the stencil used to evaluate gradient for a simulation with $R_0 = 45$, $\sigma = 0.001$. The stream-functions all correspond to the steady-state. In this data, the qualitative structure of the micro-current flow response changes

as we expose the contribution of the lattice, with inter-penetrating stream-function maxima and minima (the signature of the micro-current response ψ^2) becoming more apparent as the stencil in use is progressively refined i.e. its ψ^1 contribution removed. From table 1 and figure 5 it is clear that stencil $A_{8,4}$ corresponds to an optimum choice.

We compare the performance of the optimum anisotropic stencil $A_{8,4}$ and the widely-used compact stencil $A_{6,4}$ in figures 4 and 6. Note that a narrow interface ($\beta = 0.6$) has been used for this data, to ensure that it is relevant to practical MCLB applications. In the data of figure 6 we observe the cumulative effect on micro-current activity as measured by the compressible Stokes stream-function maximum. The blue line shows the activity associated with an ideal force and phase field, the red line a fully-coupled phase field of constant curvature and finally the green line shows the activity associated with a fully-coupled phase field with computed curvature (the typical immiscible fluid simulation). The effective segregation parameter used in this data is the representative value of $\beta = 0.6$. The adverse effect on the micro-current activity of the curvature calculation is clear. Whilst this to be expected (κ must be evaluated numerically based upon second derivatives) it is unfortunate. In the data of figure 4 we emphasise the qualitative features of the micro-current flow pattern. In this data, ideal and fully coupled phase fields, ρ^N, are subject to a force derived from compact ($A_{6,4}$) and optimum ($A_{8,4}$) stencils for the cases of constant curvature and computed curvature. Data from selected models considered in the appendix and an exact force are also included. The micro-current flow due to an exact force (sub-figure(1)) is the response to sampling, $\underline{\delta v}^{(2)}$, whereas that in (2) corresponds to $\underline{\delta v}^{(1)} + \underline{\delta v}^{(2)}$. There is good agreement between the micro-current response in the two cases of exact Lishchuk force (1) and ideal ρ^N with optimum stencil (3) note. The qualitative features of the flows in sub-figures (1)-(5) correspond to the model flow considered in case (2) of the appendix, depicted in (8). Note however, that observed circulations are much more localised on the interface. This disagreement implies that the micro-current cannot be regarded simply as a response to a tangential interfacial velocity perturbation. Sub-figures (6) and (7) show the effect of the curvature calculation and indicate that $\underline{\delta v}^{(3)}$ is fundamentally different to $\underline{\delta v}^{(1)}$ and $\underline{\delta v}^{(2)}$, as it induces an unphysical cross-interfacial flow. Such a flow is modelled in the appendix.

Let us consider that numerical error associated with sampling of an exact force distribution and its corresponding micro-current contribution, $\underline{\delta v}^{(2)}$, discussed in section 4.3. This micro-current, $\underline{\delta v}^{(2)}$, is associated with $\underline{\delta F}^{(2)}$.

By adding the negative of the model of $\underline{\delta F}^{(2)}$, defined in equations 51 and 52 i.e. removing the dissipation due to $\underline{\delta v}^{(2)}$ it should be possible to eliminate this flow. The upper panel of figure 3 shows the micro-current flow $\underline{\delta v}^{(2)}$ induced solely by error force $\underline{\delta F}^{(2)}$, which represents the lattice sampling error associated with the exact force defined in equations 30. The lower panel in figure 3 shows, with identical vector plot scaling, the corresponding micro-current when the effect of $\underline{\delta F}^{(2)}$ is removed using the model of $\underline{\delta F}^{(2)}$.

Micro-currents affecting the Lishchuk model cannot be accounted for by a tangential error force inducing a tangential flow close to the interface. This observation is supported by the fact that (i) the simple models of flow computed using the bilinear equation and appropriate boundary conditions, presented in the appendix, section A do not predict the flow patterns observed and (ii) there is a distinct sampling effect with a distinctive flow pattern, for the rectangular stream-function pattern associated with error in gradient calculation (stencil) may be clearly distinguished from that arising from the sampling effect in figure 5.

6 Conclusion

In this article we have attempted to describe, analyse and hence to reduce micro-current effects in one class of lattice Boltzmann equation simulation method describing immiscible fluids within the continuum approximation model, due to Lishchuk et al. [8]. In this model, a Laplace interface between any number of mutually immiscible fluids is maintained by a variable body force, which relies on the computation of numerical derivatives.

We have shown that the Lishchuk micro-current flow field (and the associated density adjustment) when considered in the linear, low-Reynolds number regime, may be decomposed into independent, superposed contributions arising from error terms in this body force and from its discretisation or sampling. Error force contributions which are rotational (solenoidal) are mainly responsible for the micro-current (density adjustment).

Rotational anisotropic error terms arise from numerical derivatives (which give rise to a previously observed tangential error force, [15]) but also from the sampling of the interface-supporting force. These separate contributions may be removed, either by eliminating the causal error force or by negating it, using a model of the associated viscous dissipation. While the means of eliminating the sampling contribution are over-elaborate and therefore

of restricted practical benefit, it is relatively easy to design more effective stencils with significantly improved performance, based upon the findings advanced here.

Practically, the micro-current activity arising as outlined above may be reduced by approximately three quarters by using an appropriate stencil and approximately by an order of magnitude when the effects of sampling are removed.

7 Acknowledgements

The authors acknowledge financial support from Weatherford for parts of this work.

Appendices

A Model Stokes stream-function for micro-current flow.

It is natural to seek the Stokes flow resulting from interface velocity distributions which are representative of micro-current flow. Consider a two dimensional red drop of radius R which is maintained in a circular shape by the action of interfacial tension. This drop is embedded within a blue fluid of infinite extent. The interface is sharp and assumed to be forced by some external agency into some given, purely tangential motion. This velocity boundary condition on the internal (red) and external (blue) fluids is defined shortly. The external (blue) fluid is taken to be at rest at large distance.

The motion of the internal and external fluids determined by solving the bi-linear equation [16] for incompressible flow, expressed in cylindrical polar coordinates:

$$\nabla^2\nabla^2\psi = 0, \quad \nabla^2 \equiv \frac{1}{r}\frac{\partial}{\partial r}\left(r\frac{\partial \psi}{\partial r}\right) + \frac{1}{r^2}\frac{\partial^2 \psi}{\partial \phi^2}, \tag{53}$$

where Stokes stream-function relates to the radial and tangential components of velocity as follows:

$$u_r = \frac{1}{r}\frac{\partial \psi}{\partial \phi}, \quad u_\phi = -\frac{\partial \psi}{\partial r}, \tag{54}$$

Define the tangential motion of the interface and seek separable solutions to equation 53 for both internal and external fluid which accord with this boundary condition:

$$\begin{aligned} u_\phi(r = R, \phi) &= U_0 \sin(N\phi) \\ \psi^i(r, \phi) &= R^i(r)\sin(N\phi), \quad r < R, \\ \psi^e(r, \phi) &= R^e(r)\sin(N\phi), \quad r > R, \end{aligned} \tag{55}$$

where, to respect the rectangular symmetry of the underlying two dimensional lattice $N = 4, 8, 12...$ Let us consider the internal (red fluid) solutions.

With the above, we obtain straightforwardly from equation 53 the following coupled ordinary differential equations:

$$\begin{aligned} \frac{d^2R^i}{dr^2} + \frac{1}{r}\frac{dR^i}{dr} - \frac{N^2}{r^2}R^i &= W^i \\ \frac{d^2W^i}{dr^2} + \frac{1}{r}\frac{dW^i}{dr} - \frac{N^2}{r^2}W^i &= 0, \quad r < R. \end{aligned} \tag{56}$$

Writing $W^i = Ar^n$ we obtain auxiliary equation $n^2 - N^2 = 0 \iff n = \pm N$ so that $W^i = Ar^N + Br^{-N}$ and hence:

$$\frac{d^2R^i}{dr^2} + \frac{1}{r}\frac{dR^i}{dr} - \frac{N^2}{r^2}R^i = Ar^N + \frac{B}{r^N}, \tag{57}$$

where A and B are integration constants which need not be determined (see below). The complimentary function and particular integral for R^i may be found straightforwardly. The general solution for R^i is therefore:

$$R^i(r) = \alpha r^{N+2} + \beta r^N + \frac{\gamma}{r^N} + \frac{\delta}{r^{N+2}}, \tag{58}$$

where $\alpha - \delta$ are integration constants. Clearly it is unnecessary to determine the latter in terms of A and B. A similar analysis gives an identical radial variation for the external fluid's Stokes stream-function, R^e. Eliminating singularities and divergences, we may write for the internal and external fluids the following general solution, containing four integration constants to be determined:

$$\begin{aligned} \psi^i(r,\phi) &= \left(\alpha r^{N+2} + \beta r^N\right)\sin(N\phi), \quad r < R, \\ \psi^e(r,\phi) &= \left(\gamma\frac{1}{r^N} + \delta\frac{1}{r^{N+2}}\right)\sin(N\phi), \quad r > R. \end{aligned} \tag{59}$$

We remark that the external solution will clearly meet the external boundary condition, given $N = 4, 8, 12...$ Note, equations 59 predict that micro-current response to an induced tangential velocity at the interface (equation 55), must decay more rapidly with distance away from the interface as parameter N increases.

To close the general solution in equations 59, the kinematic and dynamic boundary conditions must be applied to the internal and external solutions

at $r = R$ to write four linearly independent equations relating integration constants $\alpha - \delta$. These must then be solved. Physically, the effect of strong interfacial tension maintains a circular shape but the Laplace pressure step may be neglected when considering the velocity field. Hence, the pressure field adjustment may be determined from a closed velocity field, by integrating Stokes' equation $\underline{\nabla} P = \eta \nabla^2 \underline{v}$ expressed in the cylindrical polar form:

$$\begin{aligned} \frac{\partial p}{\partial r} &= \eta N \cos(N\phi) \left(\left(\frac{d^2}{dr^2} + \frac{1}{r}\frac{d}{dr} - \frac{(N^2+1)}{r^2} \right) \frac{R}{r} + \frac{2}{r^2}\frac{dR}{dr} \right), \qquad (60) \\ \frac{1}{r}\frac{\partial p}{\partial \phi} &= -\eta N \sin(N\phi) \left(\left(\frac{d^2}{dr^2} + \frac{1}{r}\frac{d}{dr} - \frac{(N^2+1)}{r^2} \right) \frac{dR}{dr} + \frac{2N^2}{r^2} R \right), \end{aligned}$$

with (say) the assumption of zero pressure at infinity. Note that the variation of the basis vectors $\hat{e}_r$ and $\hat{e}_\phi$ has been taken into account in equations equations 60.

We proceed to impose two choices of boundary condition sets, attempting to recover observed features of the micro-current flows. Simulations suggest that $N = 4$. Note that the choice of boundary conditions is sensibly constrained by the need for the tangential velocity of both internal and external fluids to match that assumed. Note also that in considering the micro-current, flow across the steady circular interface of continuum hydrodynamics is possible, albeit a violation of the kinematic condition.

A.1 Case 1

Let us suppose that micro-current flow is consistent with the following conditions at the interface, $r = R$ (i) a continuous tangential velocity of the form assumed (two conditions), (ii) a continuos radial flow (one condition) and (iii) continuity of tangential stress (one condition). These four conditions may be written respectively [27]:

$$\begin{aligned} \left[\frac{dR^i}{dr} \right]_{r=R} &= U_0, \qquad (61) \\ \left[\frac{dR^e}{dr} \right]_{r=R} &= U_0, \\ R^i(R) &= R^e(R), \end{aligned}$$

$$\left[\frac{d^2R^i}{dr^2}\right]_{r=R} = \lambda\left[\frac{d^2R^e}{dr^2}\right]_{r=R},$$

where the viscosity ratio $\lambda = \eta_e/\eta_i$. Substituting for R^i and R^e and using straightforward linear algebra techniques, the following solution is obtained:

$$\begin{aligned}\psi^i(r,\phi) &= U_0\left(\frac{5}{8}\left(\frac{3-\lambda}{3+\lambda}\right)\frac{r^4}{R^3} + \frac{3}{4}\left(\frac{3\lambda-1}{\lambda+3}\right)\frac{r^6}{R^5}\right)\sin(4\phi), \quad r<R, \\ \psi^e(r,\phi) &= U_0\left(\frac{3}{8}\left(\frac{\lambda-7}{\lambda-3}\right)\frac{R^5}{r^r} + \frac{5}{4}\left(\frac{3-\lambda}{\lambda+3}\right)\frac{R^3}{r^2}\right)\sin(4\phi), \quad r>R.\end{aligned} \tag{62}$$

From equations 60 the internal and external pressure fields for this case are:

$$\begin{aligned}p^i(r,\phi) &= 15\eta_i U_0\left(\frac{3\lambda-1}{3+\lambda}\right)\frac{r^4}{R^5}\cos(4\phi) + P_0, \quad r<R, \\ p^e(r,\phi) &= 15\eta_e U_0\left(\frac{3-\lambda}{3+\lambda}\right)\frac{R^3}{r^4}\cos(4\phi) + P_0', \quad r>R,\end{aligned} \tag{63}$$

where P_0 and P_0' are numerical constants. The natural choice is $P_0' = 0$. Since the ϕ dependance in these expressions precludes a continuous pressure at $r = R$. We also choose $P_0 = 0$ and accept the existence of a non-Laplace pressure step:

$$\Delta P = U_0\frac{15}{3\eta_i+\eta_e}\frac{1}{R}\left(\eta_e^2-\eta_i^2\right)\cos(4\phi). \tag{64}$$

Whilst the observed pressure adjustment $c_s^2\delta\rho$ in micro-current flow does depart from a simple Laplace pressure step, the predicted angular variation above is not observed. Hence, we suggest that stress continuity conditions do influence the micro-current velocity field.

A.2 Case 2

We next suppose that micro-current flow is consistent with the following conditions at the interface, $r = R$ (i) a continuous tangential velocity of the form assumed (two conditions) and (ii) no radial flow (two conditions). These four conditions correspond to the assumption that the internal and external

micro-current flows are independent and may be written respectively [27]:

$$\begin{aligned}\left[\frac{dR^i}{dr}\right]_{r=R} &= U_0, \\ \left[\frac{dR^e}{dr}\right]_{r=R} &= U_0, \\ R^i(R) &= 0, \\ R^e(R) &= 0.\end{aligned} \tag{65}$$

Substituting for R^i and R^e and using straightforward linear algebra techniques, the following simpler solution is now obtained:

$$\begin{aligned}\psi^i(r,\phi) &= U_0\left(\frac{r^6}{R^5} - \frac{1}{2}\frac{r^4}{R^3}\right)\sin(4\phi), \quad r < R, \\ \psi^e(r,\phi) &= U_0\left(\frac{1}{2}\frac{R^3}{r^2} - \frac{1}{2}\frac{R^5}{r^4}\right)\sin(4\phi), \quad r > R,\end{aligned} \tag{66}$$

with the corresponding internal and external pressure fields:

$$\begin{aligned}p^i(r,\phi) &= 20U_0\eta_i\frac{r^4}{R^5}\cos(4\phi), \quad r < R, \\ p^e(r,\phi) &= 6U_0\eta_e\frac{R^3}{r^4}\cos(4\phi), \quad r > R,\end{aligned} \tag{67}$$

and corresponding interfacial pressure step:

$$\Delta P = \frac{2U_0}{R}\left(10\eta_i - 3\eta_e\right)\cos(4\phi). \tag{68}$$

Again, the pressure adjustments and step predicted above do not agree with that observed in micro-current flow. More significantly, the flow calculated above (sub-figure (8) of 4) shows only broad, qualitative agreement with that observed. While the number of circulations and their approximate distribution does agree with observations, the predicted flow extends much further from the interface than that observed. We therefore infer from the investigations of this section that the observed properties of the micro-current

velocity field and corresponding pressure adjustment are inconsistent with the assumption of a Stokes flow resulting from a distribution of tangential velocity at the interface. It is likely that micro-current flow with MCLBs using Lishchuk's method must be understood as a forced response of the fluid, as set-out in section 4.

B Compressible Stokes stream-function

Write the second of equations 25 explicitly:

$$\frac{\partial}{\partial x}\left(\rho_0 u_x\right) + \frac{\partial}{\partial y}\left(\rho_0 u_y\right) = 0, \tag{69}$$

which equation is clearly identically satisfied by a scalar $\psi(x, y)$ with the property:

$$\rho_0 u_x = \frac{\partial \psi}{\partial y}, \quad \rho_0 u_y = -\frac{\partial \psi}{\partial x}. \tag{70}$$

By taking its material derivative, scalar $\psi(x, y)$ may be shown to be constant following steady motion:

$$\frac{D\psi}{Dt} = \frac{\partial \psi}{\partial t} + u_x \frac{\partial \psi}{\partial x} + u_y \frac{\partial \psi}{\partial y} = -\frac{1}{\rho_0}\frac{\partial \psi}{\partial y}\frac{\partial \psi}{\partial x} + \frac{1}{\rho_0}\frac{\partial \psi}{\partial x}\frac{\partial \psi}{\partial y} = 0, \tag{71}$$

and hence contours $\psi(x, y) = \textit{constant}$ may be used to depict streamlines, for steady compressible flow.

C Figures and Captions

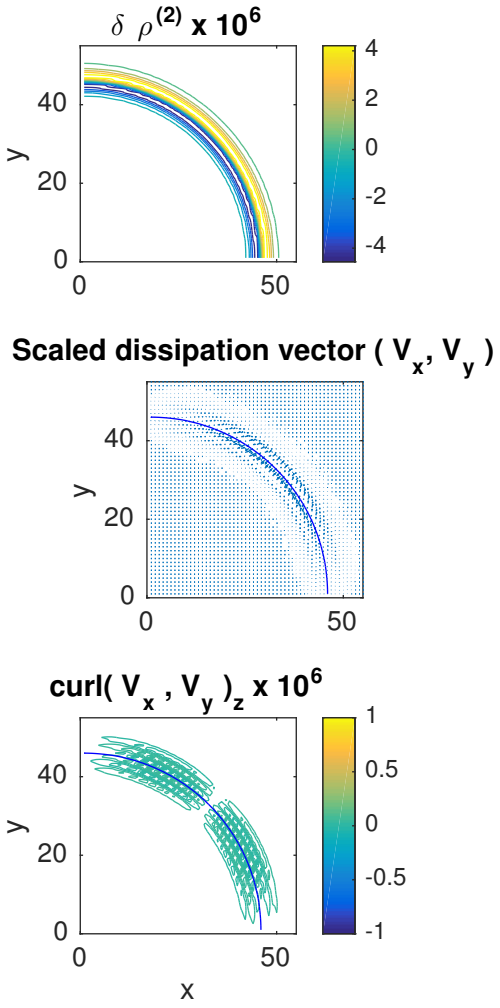

Figure 1: The upper figure corresponds to the density adjustment, the middle figure is the two-dimensional micro-current dissipation field computed from equation 27 (which has been scaled for display) and the bottom figure is the z-component of its curl. These data correspond to the idealised, centripetal interface force distribution given in equation 30. The solid line in each figure shows the location of what would be the centre of the interface at $R = 45$ lattice units, with its centre at the origin. The effective segregation parameter $\beta = 0.6$.

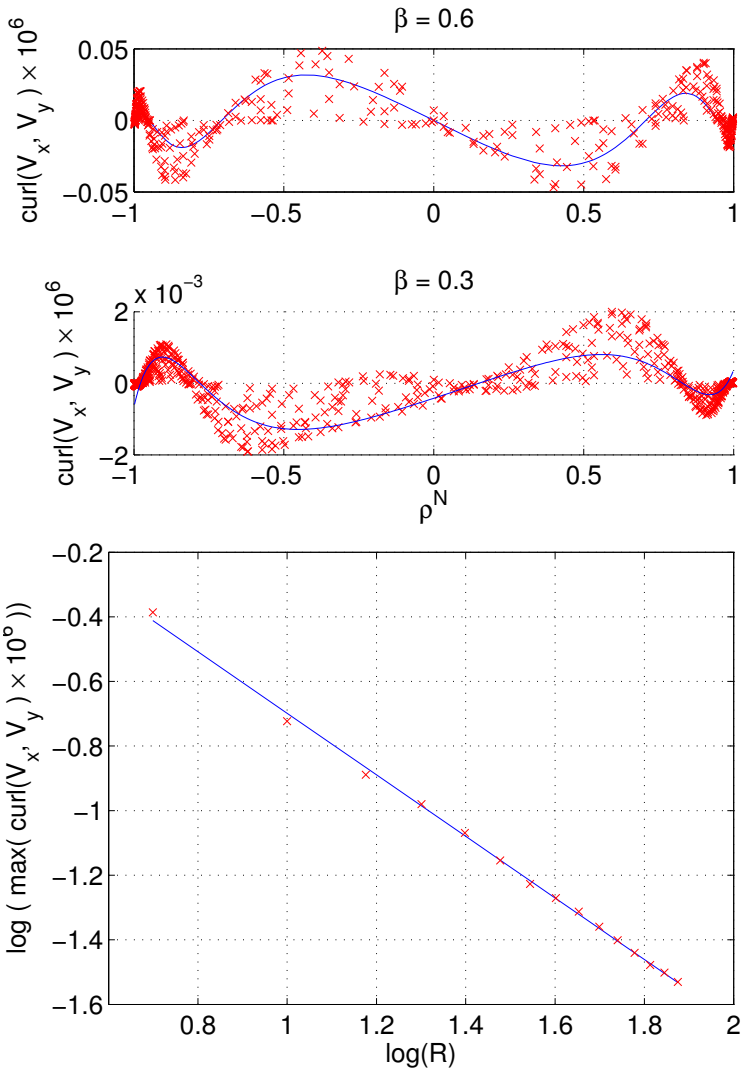

Figure 2: Upper and middle figures. For the indicated value of β, discrete points show the measured curl of the micro-current dissipation (equation 27: see also figure 1) plotted against ρ^N, for lattice points $\phi \in [0, \frac{\pi}{4}]$. Data density increases as $|\rho^N| \to 1$ as there are more lattice points located in the bulk phases. Continuous line is the empirical fit. Lower figure. Amplitude of the curl of micro-current dissipation versus radius of curvature, R. The continuous line is optimum fit $y = -0.953x + 0.254$.

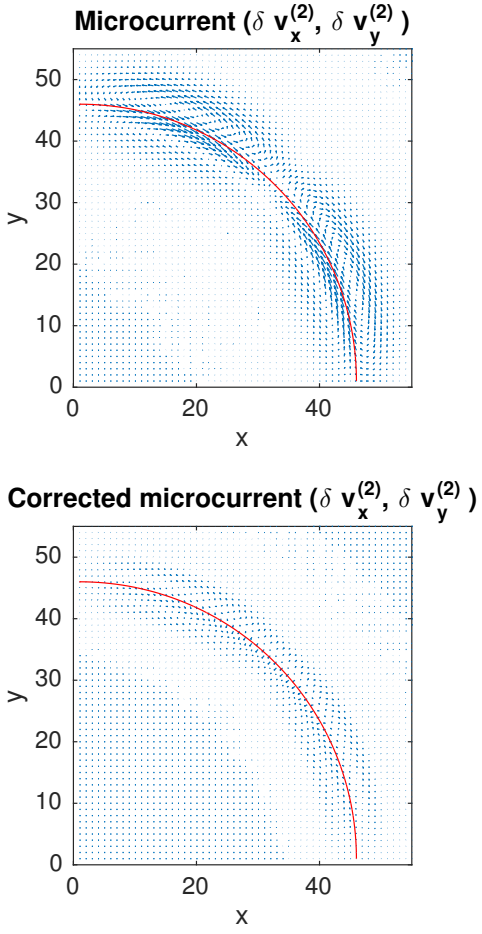

Figure 3: Upper figure. Scaled micro-current flow $\underline{\delta v}^{(2)}$ induced solely by $\underline{\delta F}^{(2)}$, the sampling error associated with an exact Lishchuk force. Lower figure. The corresponding micro-current displayed using identical vector plot scalings when the effect of $\underline{\delta F}^{(2)}$ is removed as discussed in the text. The parameters for this data as $\beta = 0.3$, $R = 45$. The solid red contour corresponds to the centre of the interface.

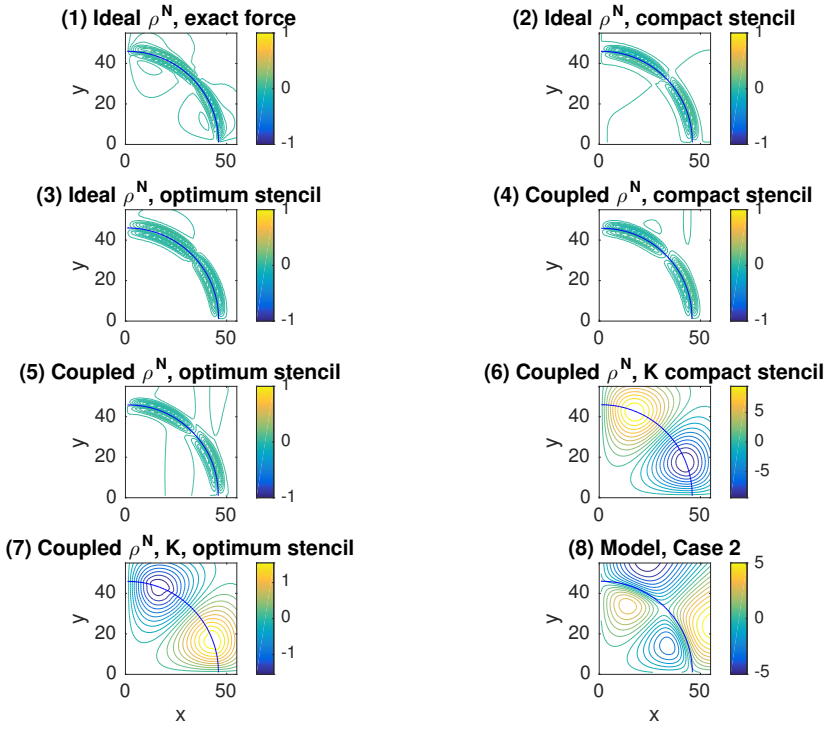

Figure 4: Contours of the compressible Stokes stream-function of the micro-current flow defined in equation 71, for a range of identified stencils applied to the idealised centripetal interface force distribution given in equation 30 and to a simulation with a fully coupled phase field. Also shown in parts (5)..(8) are the flow patterns associated with the curvature calculation.

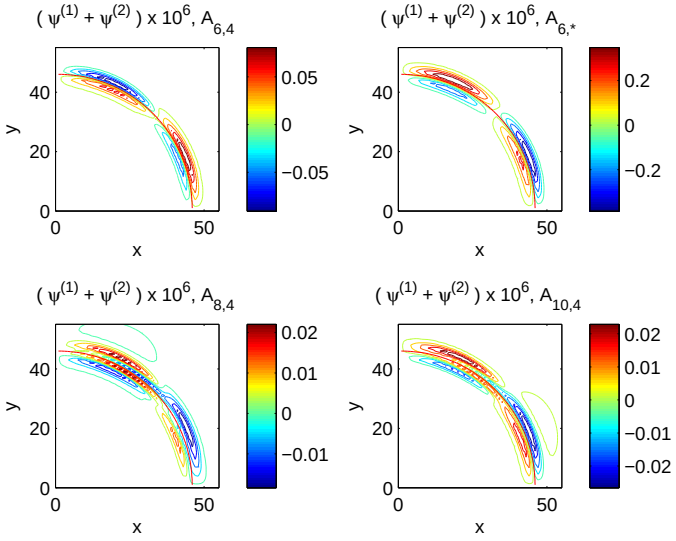

Figure 5: Comparison of micro-current activity measured by the compressible Stokes stream-function for the indicated stencil. See also table 1. Broadly, as the contributions of the error terms in a stencil are progressively eliminated a residual activity is exposed, the flow pattern of which is distict. Note, however, eliminating error terms $\epsilon^{(4)}$ promotes micro-current (compare first two panels), due to the increased weighting of anisotropic terms in $\epsilon^{(6)}$. The solid line in each figure shows the location of what would be the centre of the interface at $R = 45$ lattice units, with its centre at the origin. The effective segregation parameter $\beta = 0.6$.

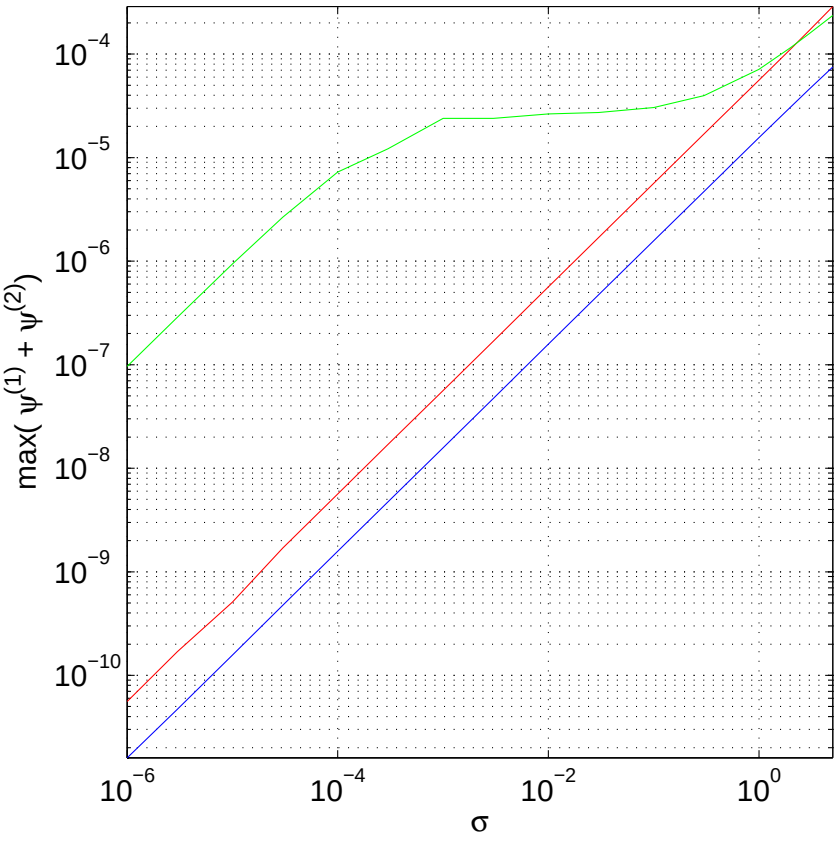

Figure 6: Comparison of micro-current activity measured by the compressible Stokes stream-function for an ideal Lishchuk force and phase field (blue line), an fully-coupled phase field of constant curvature (red) and fully-coupled phase field with computed curvature (green). The effective segregation parameter $\beta = 0.6$.

References

[1] A. K. Gunstensen, D. H. Rothman, S. Zaleski and G. Zanetti, Phys. Rev. A 43(8), pp4320-4327 (1991).

[2] M. R. Swift, W. R. Osborn and J. M. Yeomans, Phys. Rev. Lett. 75(5), pp830-833. (1995).

[3] M. R. Swift, E. Orlandini, W. R. Osborn and J. M. Yeomans, Phys. Rev. E **54**(5), pp5041-5052, (1996).

[4] A. J. Wagner, Phys. Rev. E. 74, 056703 (2006)

[5] Q. Li and A. J. Wagner Phys. Rev. 76 E. art. no. 036701 (2007) and references therein.

[6] A. J. Wagner and C. M. Pooley, Rev. 76 E. art. no. 056703 (2007) and references therein.

[7] X. W. Shan and H. D. Chen, Phys. Rev. E, 49 pp2941 (1994)

[8] S. V. Lishchuk, C. M. Care and I. Halliday, Phys. Rev. E 67(3), 036701(2), (2003).

[9] I. Halliday, A. P. Hollis and C. M. Care, Phys. Rev. E, 76 026708 (2007).

[10] M. M. Dupin, I. Halliday and C. M. Care, Phil. Trans. Roy. Soc. A. 362, pp1775-1761 (2004).

[11] M. M. Dupin, I. Halliday and C. M. Care, Medical Engineering and Physics 28 pp13-18 (2006).

[12] T. J. Spencer, I. Halliday and C. M. Care, Phys. Rev.E 82 066701 (2010).

[13] T. Lee and P. F. Fischer, Phys Rev. E 74, 046709, (2006)

[14] C. M. Pooley and K. Furtado, Phys. Rev. 77, 046702 (2008)

[15] X . Shan, Phys. Rev. E, 73 -47701 (2006).

[16] L. Landau and E. M. Lifshitz, Fluid Mechanics, Sixth Edition, Pergamon Press.

[17] U D'Ortona, D. Salin, M. Cieplak, R. Rybka and J. Banavar Phys. Rev. E 51, pp3718 (1995)

[18] I. Halliday, S. V. Lishchuk, T. J. Spencer, G. Pontrelli and C. M. Care, Phys. Rev. E, 87, 023307 (2013) and references therein.

[19] X. He, S. Chen and G. D. Doolen, J. Comp. Phys. 146 pp282 (1998).

[20] Z. Guo, C. Zheng and B. Shi, Phys. Rev. E, Vol 65 046308 (2002).

[21] Q. Li, K. H. Luo and X. J. Li, Phys Rev E, 86, 016709 (2012).

[22] A. L. Kupershtokh, D. A. Medvedev and D. I¿ Karpov, Comput. Math. Appl. 58 pp965 (2009).

[23] P. L. Bhatnagar, E. P. Gross and M. Krook, Phys. Rev 94 pp511 (1954).

[24] Y. H. Qian, D. d'Humières and P. Lallemand, Europhys. Lett. **17**, 479 (1992).

[25] S. Succi, *The lattice Boltzmann equation for fluid mechanics and beyond*, Clarendon Press (2001).

[26] S. Hou, Q. Zou, S. Chen, G. Doolen and A. C. Cogley, J. Comp. Phys. 118 pp329-345 (1995).

[27] J. Happel and H. Brenner, *Low Reynolds Number Hydrodynamics* Second Edition, Noordhoff International Publishing (1965)